Introduction

"The reason for this proposal is our belief that the correct understanding and solution of many problems in reflection seismology depend on the more rigorous and exact analysis that can be obtained by faithfully solving the wave equation." - Jon Claerbout, proposal to initiate the Stanford Exploration Project, 1973.

0.1 Why migration to zero offset?

Migration to zero offset (MZO) is an operation that transforms a common-offset section into a zero-offset section. In constant velocity media MZO is equivalent to the normal moveout correction (NMO) followed by the dip moveout correction (DMO). For variable velocity media NMO and DMO do not transform a constant-offset section into a zero-offset section, and consequently there is a need for a new operator definition, i.e. MZO.

Obtaining an image in a variable velocity media requires various forms of prestack depth migration which are wave-equation derived algorithms. NMO, on the other side, is a data derived technique that attempts to align the reflections in the best way for enhancing common-midpoint stacking. DMO bridges the gap between data driven imaging techniques and wave-equation imaging techniques, but is analytically defined only for constant velocity media. MZO tries to narrow, or even close the gap between wave-equation imaging techniques like prestack migration and data driven imaging techniques like NMO by defining a wave-equation derived operator valid for variable velocity media.

The next section gives a list of enhancements to the data that DMO or MZO offers. From a computational point of view, one of the most valuable properties of the MZO operator is that it is a spatially compact operator. Another important property of the MZO operator is that it images in time and therefore it can handle implicitly velocity and anisotropy structures. Compared to the prestack migration operator that increases in aperture with depth, the MZO operator decreases in aperture with velocity and depth. This in turn ensures that data is spread or summed over smaller distances and therefore the opportunity to damage the information using the wrong velocity or the wrong amplitudes is diminished. This is an important property, useful

for amplitude versus offset (AVO) studies or in general any offset comparison techniques. This property also promises a computationally cheaper prestack migration alternative.

0.1.1 DMO and MZO kinematics

The most general wave-equation definition of the MZO operator is the one proposed by Deregowski and Rocca (1981) who describe migration to zero offset as the combination of prestack migration followed by zero-offset modeling. A more accurate description for MZO, if we assume the modeling operator to be a forward operator, would be the combination of prestack inversion followed by zero-offset modeling, but these are secondary details to understanding the physical nature of MZO.

Following Deregowski and Rocca's definition of MZO, I was surprised to find out in my earlier work (Popovici and Biondi, 1989; Popovici 1990), that the impulse response of the MZO operator in media with only depth velocity variations can be very different from the impulse response of the combined NMO plus DMO; in particular, triplications appear in the kinematics of an operator that was supposed to be very simple and nicely behaved. The difference between the variable velocity impulse response of the MZO and the standard NMO and DMO impulse response was the first reason that motivated me to look further into this research topic.

Figure 0.1 shows the difference between the impulse response of the NMO and DMO operator and the kinematics of the MZO operator. The velocity model is a two layer model, with an upper velocity of 1500 m/s and a lower velocity of 3000 m/s. The left panel shows the standard NMO and DMO impulse response, while the right panel shows the impulse response of the MZO developed in this thesis. Overlayed is the more accurate impulse response computed using the Deregowski and Rocca definition by doing prestack migration followed by zero-offset modeling using finite difference traveltimes. The Deregowski and Rocca impulse response shows triplications due to the transition zone between the two velocity layers.

The difference in the DMO operator and the MZO operator is significant even for a very simple depth-variable velocity model. The impulse response on the right, which shows a very good kinematic equivalence to the Deregowski and Rocca operator, was computed using the MZO phase-shift algorithm described in this thesis.

It is known that for a linear increase in velocity DMO applied after NMO with the correct V_{rms} undercorrects the diffraction branches (Hale, 1984). For the simple two layer velocity model shown in Figure 0.2, the effect of DMO on diffraction hyperbolas is opposite to the effect on dipping reflectors. For dipping reflectors DMO overcorrects the curvature, as shown in Figure 0.3a. As a result, techniques to adapt the DMO for variable velocity which are based on squeezing the DMO ellipse will align only one event correctly while degrading the alignment for the other.

Figure 0.2a shows three dipping reflectors in a medium with the depth variable velocity shown in Figure 0.2b. Figure 0.3a shows the effect of DMO on the synthetic

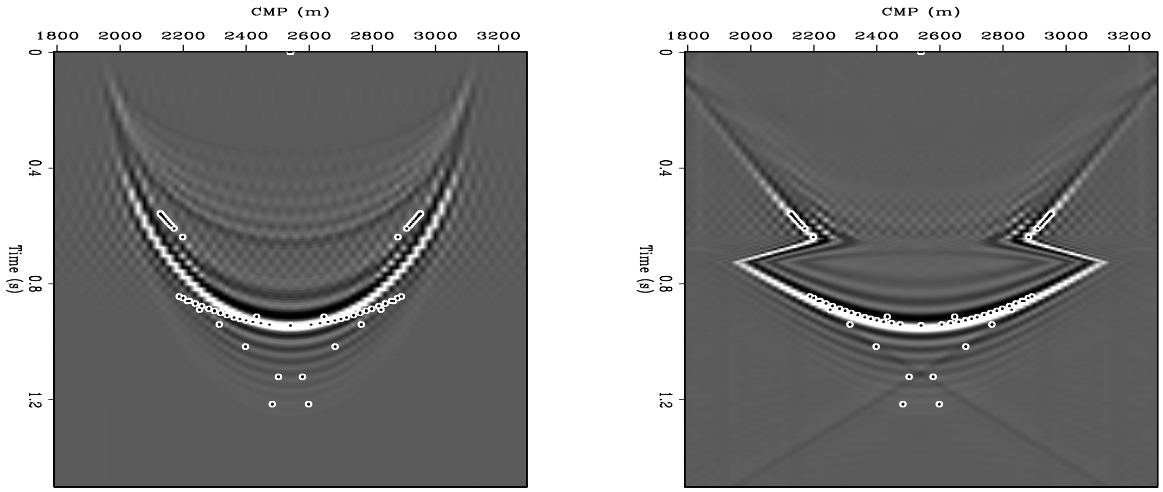

Figure 0.1: The impulse response of the DMO plus NMO operator compared to the impulse response of the MZO operator in a 2 layer medium. The kinematics of the MZO impulse response computed using the Deregowski and Rocca definition are overlayed on top. intro-DMOandMZOimps [CR]

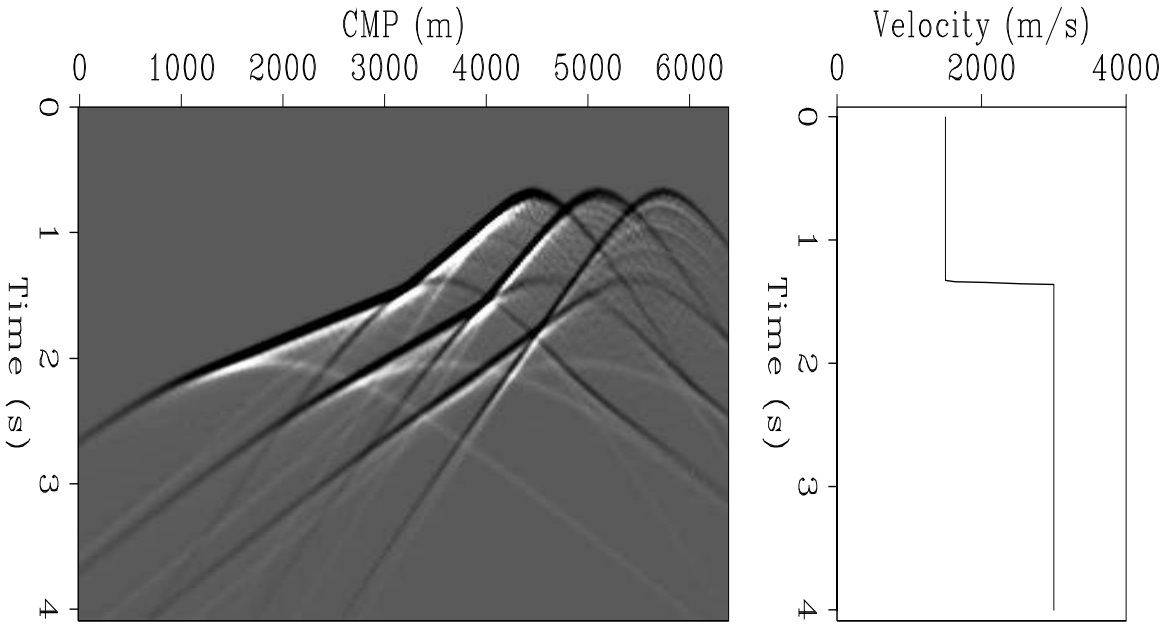

Figure 0.2: Zero-offset section and the velocity model.
a. Zero-offset section showing three dipping reflectors in a two layered medium and the diffractions associated with the reflector ends.
b. Interval velocity in time. intro-COandvt [ER]

common-offset data. The events sloping upward are dipping reflectors while the events sloping downward are diffraction hyperbola branches. After applying DMO with the squeezing correction γ, the reflector alignment is better while the diffraction alignment is worse. The conclusion is that for some depth-varying velocity media, simple modifications to the DMO algorithm that do not take into account the multiple branching of the operator could degrade the stacked image.

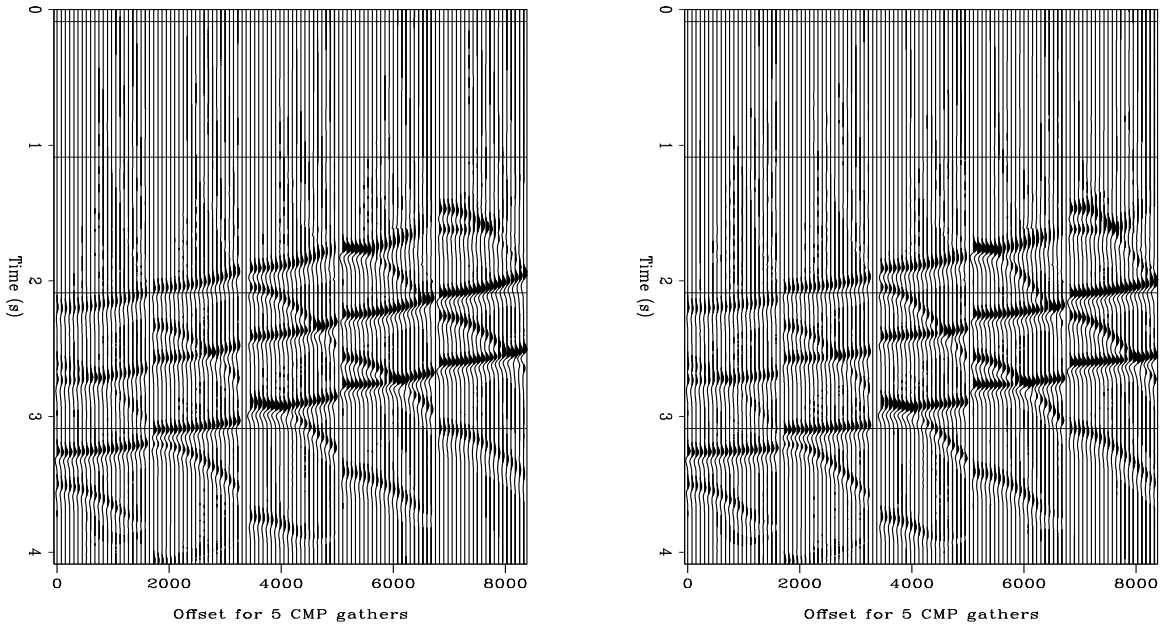

Figure 0.3: Standard DMO, and DMO using the γ correction.
a. Several CMP gathers after NMO and DMO.
b. Several CMP gathers after NMO and DMO using the γ correction. intro-DMOwgamma [CR]

0.1.2 DMO in the North Sea

An area of extensive seismic exploration, the Central Graben in the North Sea, seems to present a difficult problem for constant velocity DMO. In imaging seismic data from such an area, an accurate depth-variable MZO could bring improvements in stacking the steeply dipping flanks of domes.

Hawkins (1994) describes the geology of the Central Graben in the North Sea, where a dramatic velocity gradient seems to require a good v(z) DMO. A typical Central Graben velocity profile consists of a water layer, followed by about 3000 m of Tertiary and younger sediments with an average velocity of 2000 m/s, followed by a hard Chalk with velocities increasing abruptly to 4000 m/s, and in some intervals to over 5000 m/s. In this background velocity are several salt domes that seem to present a serious problem to the geophysicist trying to image their flanks using standard DMO methods.

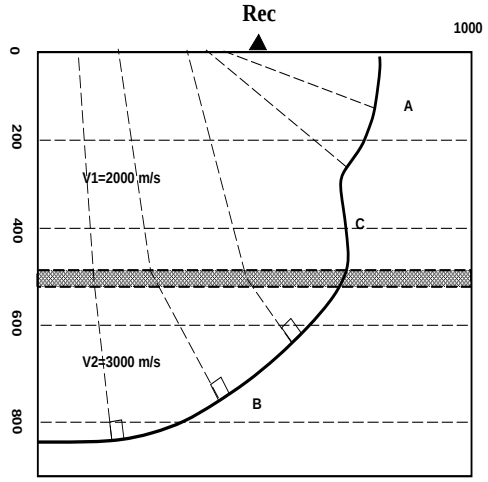

Figure 0.4: An isochrone that generates a MZO impulse response in depth-variable velocity media. The isochrone corresponds to the prestack migration kinematics of an impulse at 1.1 seconds and a half offset of 580 m. The dashed lines represent the zero-offset rays. intro-NSeaIso [NR]

Figure 0.4 shows the kinematics of the traveltimes in a constant-offset section and a step function interval velocity profile that is similar to the North Sea Central Graben velocity profile. The thick line in Figure 0.4 represents the right half of an isochrone in the constant-offset traveltime map. There are three sections along the isochrone, that can be separated from a kinematic point of view. The branch in Figure 0.4, corresponding to the area A, is associated with traveltimes going only through the top velocity layer. The branch corresponding to the area B is associated with traveltimes traversing both velocity layers. The branch corresponding to the area C are head waves, propagating through the first velocity layer and the gray area which represents a transition layer between the two velocity horizons.

The DMO operator constructed by raytracing at 90 degrees from the isochrone, has contributions from each branch of the isochrone. The dashed lines in Figure 0.4, represent the zero-offset rays. The traveltimes along the rays give the time correction for the MZO operator, while their intersection with the surface gives the spatial correction.

The zero-offset rays corresponding to branch A in Figure 0.4 contribute to the branch A of the MZO operator in Figure 0.5. In the same way, the branch B in Figure 0.4, is mapped on the MZO operator in the area B. The triplications of the MZO operator in the area C are due to the head waves that are contoured by the branch C on the isochrone in Figure 0.4.

0.1.3 The new MZO method

Central to this thesis is a new equation for MZO, that I derive analytically from the double square root equation by extracting the zero-offset migration operator. The new phase-shift formulation for MZO is expressed as:

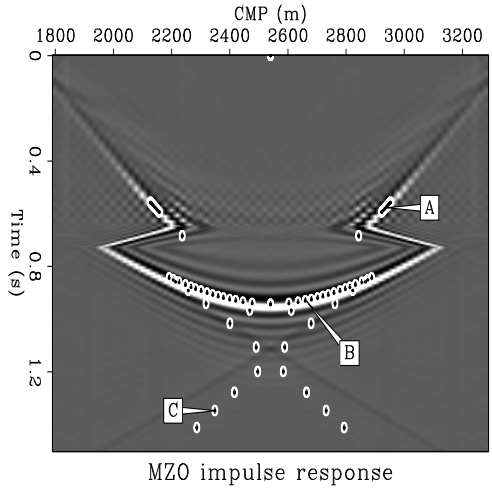

Figure 0.5: The MZO operator with traveltime kinematics superimposed on phase-shift MZO kinematics. The branch A corresponds to rays traveling in the upper velocity layer, while the branch B corresponds to rays traveling through both velocity layers. The triplications in branch C are due to the transition zone. intro-MZOvzex [CR]

$$p_0(t_0,k_y)=\int dk_h \int d\omega\; e^{-i\frac{\omega t_0}{2}\left[\sqrt{(1-Y)^2-H^2}+\sqrt{(1+Y)^2-H^2}\right]}p(\omega,k_y,k_h). \qquad (0.1)$$

where I used the customary notations

$$H=\frac{vk_h}{2\omega} \text{ and } Y=\frac{vk_y}{2\omega},$$

and $p(\omega,k_y,k_h,z=0)$ is the 3-D Fourier transform of the field $p(t,y,h,z=0)$ recorded at the surface, using Claerbout's (1985) sign convention:

$$p(\omega,k_y,k_h,z=0)=\int dt\; e^{i\omega t}\int dy\; e^{-ik_y y}\int dh\; e^{-ik_h h}p(t,y,h,z=0).$$

The field $p_0(t_0,k_y)$ represents the zero-offset data in time and in common-midpoint wavenumber coordinates.

Equation (0.1) represents a novel form of migration to zero-offset. It is analytically derived from the wave equation, and therefore it treats correctly the kinematics of the DMO+NMO operator and is consistent in amplitude with the double square root (DSR) equation. It is similar in form to the DSR equation, since the complex exponential operator has the sum of two square roots in its phase. However, downward continuation is performed in time in the case of the MZO operator, not in depth as with DSR migration. This difference suggests the use of a time-varying velocity, which could be more convenient since the $v(x,t)$ velocity is information obtained from surface data and requires fewer assumptions about structure.

Another application in which MZO has potential advantages over full prestack migration is velocity estimation. The velocity function assumed for applying MZO influences the alignment in time of the reflections over offset but not their absolute position. In contrast, the choice of the migration velocity influences the absolute position of the reflections (Fowler, 1988).

Because migration to zero-offset can be used to focus the image without knowing the complete velocity structure, anisotropy can be also included in the focusing step (Dellinger and Muir, 1988). Additionally, the focusing analysis can be used to get a better time interval velocity estimation. Equation (0.1) is velocity dependent and the velocity can be used as a parameter for focusing analysis over different offsets, not only for zero-offset. Such an analysis will implicitly handle the anisotropic velocity variations and the depth structure velocity since it is performed in time and not in depth.

Equation (0.1) also provides a link between the wave-equation and "true amplitude" DMO formulations. Chapter 2 shows that the DMO formulation extracted analytically from the DSR prestack migration equation coincides kinematically to the standard DMO algorithms. However, from an amplitude point of view, DMO extracted from the DSR equation without any approximations, does not correspond to the generally accepted definitions of "true amplitude" DMO (Black et al.,1993; Bleistein 1990). This observation can be used for deriving a new DSR formulation for prestack migration to better handle the migration amplitudes.

To summarize, my motivation for examining the variable-velocity migration-to-zero-offset imaging method is manyfold. A better understanding of the wave-equation nature of the MZO through the DSR formulation. A formal derivation of DMO and MZO from the wave equation. The surprising difference between the MZO kinematics and the NMO plus DMO kinematics and the inability of the various corrections to standard DMO to handle operator multi-branching. The real data challenge presented to DMO algorithms in areas with strong velocity gradients.

0.2 Background and history of DMO processing

Since its introduction in the late seventies, the dip moveout correction has become a standard processing step in seismic data imaging. Migration to zero offset processing is a generalization of the DMO process. As this thesis will prove, MZO has all the advantages of DMO processing and is more accurate. Among the many advantages of the DMO step, perhaps the greatest, is its robustness. It requires few parameters and almost always improves the output section. Moreover, applying a succession of DMO, NMO, stacking, and zero-offset migration can replace the more expensive sequence of prestack migration for each offset and stacking. However, the migration to zero-offset is not the only improvement that DMO delivers to the seismic section. Ideally, DMO processing enhances the data in numerous ways stated best in the following list by Deregowski (1986), to which Hale (1991) added item 11:

1. Migrate each trace to zero offset so that each common-offset section becomes identical to a zero-offset section.

2. This in turn implies that post DMO, but prestack, common-midpoint gathers contain the reflections from common depth points as defined by normal incidence rays. That is, reflector point dispersal for nonzero offset traces is removed.

3. Cross line ties are improved because a zero-offset trace is the same regardless of the direction of the offsets from which it is derived.

4. Dead traces are interpolated according to local time dips without those dips having to be estimated by a separate operation.

5. Coherent noise with impossibly steep dip is removed, without the artificial alignments often associated with dip filters. At the same time steeply dipping fault planes are better imaged alongside horizons with smaller dips.

6. The signal-to-noise ratio is improved, especially at high offsets.

7. Stacking velocities become independent of dip so that correct stacking of simultaneous events with conflicting dips is made possible.

8. Velocity analysis is improved and provides velocities that are more appropriate for migration as well as stacking.

9. Diffractions are preserved through the stacking process so as to give improved definition of discontinuities after post-stack migration.

10. Post-stack migration becomes equivalent to prestack time migration, but at considerably less expense.

11. (Hale) Amplitude versus offset studies are more meaningful after DMO because reflections in a common-midpoint gather have common specular reflection points.

These advantages justify the wide application of DMO processing in the last decade.

Historically, DMO was first presented at the 48th SEG Meeting in San Francisco by Judson et al. (1978), who called their process DEVILISH (dipping event velocity inequalities licked). Though little detail was given about the actual implementation, DEVILISH used a finite-difference operator to perform a dip-limited DMO correction.

Yilmaz and Claerbout (1980) proposed a processing sequence called *prestack partial migration* (PSPM) that represents the difference between the migration before stacking and the conventional data processing scheme of NMO correction, stacking, and zero-offset migration. The basis of their paper is Yilmaz's thesis (1979), which also has a very elegant mathematical derivation of the double-square root (DSR) prestack migration equation, derived directly from the wave equation.

Deregowski and Rocca (1981) proposed an integral formulation for DMO processing by considering the impulse response of the DMO+NMO operator as a transformation from constant offset to zero offset, using raytracing arguments. This opened the way for the development of a flexible DMO method: DMO as an integral (Kirchhoff) method. It correctly determines the kinematics of the impulse response, though the amplitude of the operator continues to be an area of research on which different schools of thought have not reached agreement.

Hale (1983) proposed a method for performing DMO processing by Fourier transform that is accurate for all dips and offsets in constant velocity and also derived extensions of DMO processing to approximate slow velocity variations with depth. In the third chapter of his thesis, Hale laid the foundations for analytically deriving the DMO from the DSR prestack migration equation. These foundations served as the starting point for the work this thesis presents.

Jakubowicz (1984) proposed an efficient version of DMO by Fourier transform by decomposing the data into a discrete number of dips that are each processed with their own dip-dependent stacking velocity. The dips are then added together after dip filtering so that each dip contributes only once to the final CMP stack. Moreover, Meinardus and Schleicher (1991) showed how his method can be used in 3-D depth-variable velocity media by changing the NMO velocities with the azimuth of the source-receiver configuration.

Biondi and Ronen (1987) proposed an algorithm to perform DMO in shot profiles by multiplying the data in the Fourier domain by a time- and space-invariant shot-DMO operator. These conventional DMO operators are kinematically correct when velocity is constant and approximately correct when velocity increases linearly with depth (Hale, 1983), but they cannot be applied when velocity varies laterally and depth prestack migration is required to image the structure.

When velocity varies rapidly with depth or varies laterally, DMO processing fails (Black et al., 1985). The direct solution to these problems is full migration before stacking. However, this process is computationally expensive because it requires a much greater volume of data to be migrated than post-stack migration. There exist approximations to the DMO algorithms for slow increase of velocity with depth (Deregowski and Rocca, 1981; Hale, 1983; Popovici, 1990; Hale and Artley, 1993; Artley, 1992). However, for fast velocity gradients, velocity that decreases with depth, or laterally varying velocity, the present DMO algorithms fail to provide an accurate solution to the zero-offset transformation problem. Jakubowicz (1990) notes that "When the problems encountered in CMP stacking are primarily due to lateral velocity variations, there is at present, alas, no alternative to applying some form of depth migration before stack." The new MZO algorithm developed in this thesis addresses precisely this issue.

Migration to zero-offset (MZO) combined with zero-offset migration could be a faster alternative to prestack migration. Until recently, though, MZO theory was only developed for constant velocity media with some approximations regarding the depth-variable velocity case (Meinardus and Schleicher, 1992; Hale and Artley, 1992). So far, accurate depth MZO algorithms have been more expensive than actual prestack depth migration (Popovici, 1990; Artley, 1992) and therefore are rarely used. The new MZO algorithm this thesis proposes works not only for depth variable velocity media but also for laterally variable velocity media, and is faster than prestack migration.

0.3 Fundamentals of DMO kinematics

The following sections are a tutorial intended as an introduction to the fundamentals of DMO processing, discussing first the kinematics of DMO and second the first-order amplitude theory of DMO by Fourier methods. Readers familiar with the basic concepts of DMO can skip directly to the next chapter, which presents the theory of MZO processing.

0.3.1 The need for DMO processing

The need for dip-moveout processing arose because of the problem of stacking traces that share the same common midpoint (CMP). Figure 0.6 shows the geometry of a CMP section over a flat layer. In a CMP section, traces are sorted so they share the same midpoint for different locations of the source and receiver. In this configuration, when only flat layers are present, the reflections come from a single point situated under the CMP.

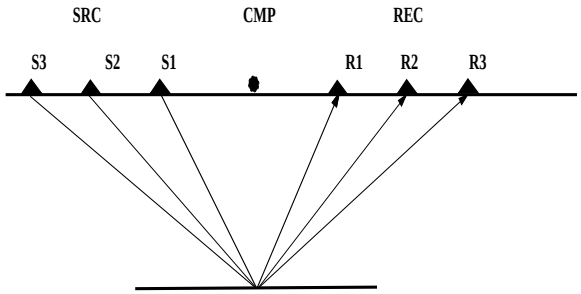

Figure 0.6: Geometry of a CMP gather over a flat layer. intro-CMPgeonodips [NR]

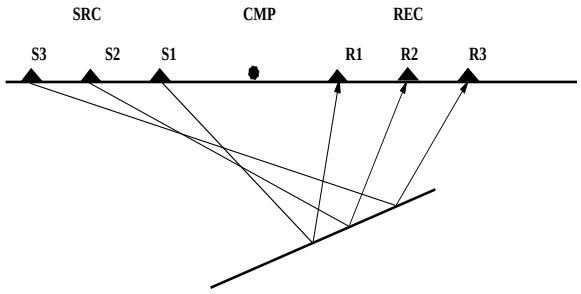

Figure 0.7: Geometry of a CMP gather over a dipping layer. intro-CMPgeodips [NR]

Figure 0.7 depicts the geometry of a CMP section over a dipping layer. In this case the reflections do not come from the same point, but move updip as the offset between source and receiver increases.

CMP stacking assumes that reflections come from horizontal layers. Under this assumption, the normal-moveout correction flattens the hyperbolas in a CMP gather to horizontal lines. After NMO, traces belonging to the same CMP are summed together (stacked) to enhance the reflected signal and attenuate the noise.

Problems appear when multiple dipping events occur in a section. Figure 0.8a combines the geometry in Figures 0.6 and 0.7 for multiple CMPs. Each hyperbola corresponds to a CMP section over a dipping layer and a flat layer. The third axis (CMP axis) was suppressed by projecting the hyperbolas of different CMP sections into a single plane. As the CMP moves updip, the hyperbolas corresponding to the dipping layer appear closer to the surface, while the ones corresponding to the flat layer are unchanged.

A dipping reflector in a CMP section (see Figure 0.8a) produces a reflection hyperbola as the next section proves. The NMO velocity necessary to flatten the hyperbolas originating from reflections on the dipping layer is higher than the real velocity.

Figure 0.8a shows several CMP gathers containing reflections from a dipping layer and a horizontal layer. After NMO with the real velocity, the hyperbolas corresponding to the flat layer become straight lines (Figure 0.8b). After stacking (Figure 0.8c), the horizontal event is preserved at the expense of the dipping event.

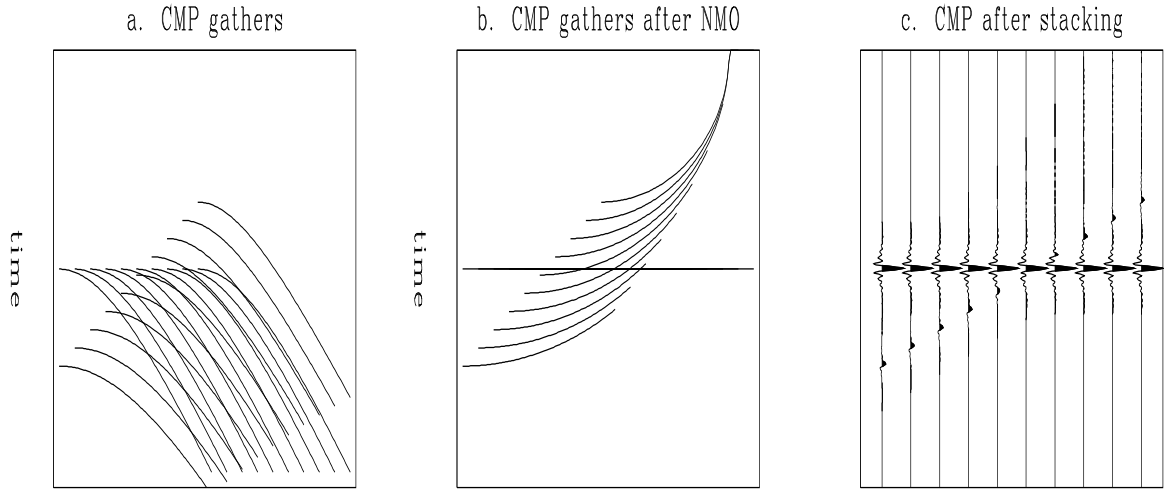

Figure 0.8: Effect of CMP stacking with real velocity on dipping reflectors.
a. Several CMP gathers for a flat layer and a dipping layer. The third axis (CMP) is suppressed by projecting all gathers into one.
b. The CMP gathers after NMO with medium velocity (v_{real}); the hyperbolas from the horizontal event are flattened.
c. Traces after stacking for the same CMP. intro-CMPnmoEx1 [ER]

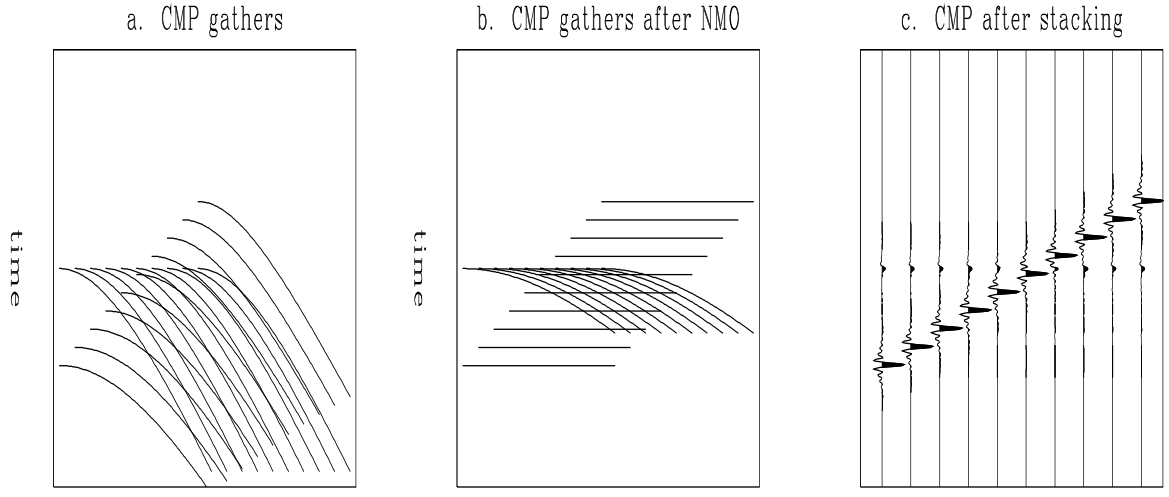

Figure 0.9: Effect of CMP stacking with velocity ($v_{nmo} = v_{real}/\cos\theta$) on horizontal reflectors.
a. Several CMP gathers for a flat layer and a dipping layer. The third axis (CMP) is suppressed by projecting all gathers into one.
b. The CMP gathers after NMO with higher velocity; the hyperbolas from the dipping event are flattened.
c. Traces after stacking for the same CMP. intro-CMPnmoEx2 [ER]

Figure 0.9a shows the same CMP gathers as in Figure 0.8a but the NMO velocity used to flatten the hyperbolas from the dipping reflector is higher than the real medium velocity. In Figure 0.9b NMO is performed with the higher velocity necessary to flatten the hyperbolas corresponding to the dipping event. After stacking

(Figure 0.9c), the dipping event is preserved at the expense of the horizontal layer. It is obvious that the NMO correction with a single velocity, combined with CMP stacking, acts as a dip filter. The result is a degradation of the final image when conflicting dips are present.

0.3.2 The NMO velocity

Figure 0.10 shows a dipping reflector and the position of the source, geophone, and CMP. The common-offset traveltime from the source at point **A** to the receiver at point **B** is represented by the sum of the segments **AR** and **RB**. The zero-offset traveltime from the CMP to the reflector and back is given by the segment **FG**. The dipping reflector serves as the axis of symmetry for the figure.

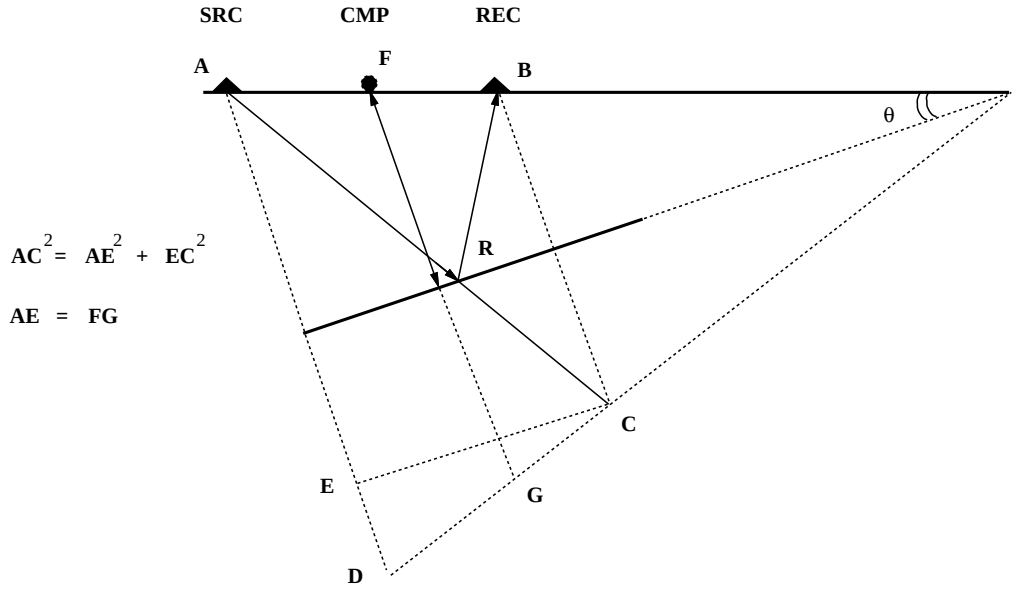

Figure 0.10: Dipping reflector in a constant velocity medium. The dipping angle is θ. The raypath from the source to the receiver is represented by the segments **AR** and **RB**. The zero-offset raypath is equal to the segment **FG**. intro-dmofig1 [NR]

For the geometry in Figure 0.10, we have

$$\mathbf{AC} = \mathbf{AR} + \mathbf{RB} = vt_h,$$

where v is the velocity of the medium, and t_h is the shot-receiver traveltime. The segment **FG** (which has the length of the zero-offset raypath) is equal to the segment **AE**, as can be seen from Figure 0.10 and the trapezoid **ABCD**:

$$\mathbf{FG} = (\mathbf{AD} + \mathbf{BC})/2 = \mathbf{BC} + \mathbf{ED} = \mathbf{AE}.$$

In the triangle $\triangle\mathbf{AEC}$, using Pitagora's identity we can write the relations

$$\mathbf{FG}^2 = \mathbf{AE}^2 = \mathbf{AC}^2 - \mathbf{EC}^2 = (vt_h)^2 - (2h\cos\theta)^2, \tag{0.2}$$

where θ is the angle of the dipping reflector, and $2h$ is the distance between source and receiver. Finally, dividing the segments with the velocity, we obtain the zero-offset traveltime from the CMP to the reflector:

$$t_0^2 = t_h^2 - \left(\frac{2h\cos\theta}{v}\right)^2 = t_h^2 - \left(\frac{2h}{v_{nmo}}\right)^2. \tag{0.3}$$

We can easily see that in equation (0.3) the expression for t_h is a hyperbola, with the top at t_0. The NMO velocity necessary to flatten the hyperbola for a dipping reflector is

$$v_{nmo} = \frac{v}{\cos\theta}. \tag{0.4}$$

Since the cosine function is always smaller than or equal to one, the NMO velocity v_{nmo} necessary for the best stacking is greater than or equal to the medium velocity.

0.3.3 Extending NMO to DMO

The dip-moveout correction is in fact an extension of the normal moveout correction used when dips are present. In the presence of only horizontal layers, NMO tries to correct the effect of the offset and transform all the common-offset sections into zero-offset sections. The DMO+NMO correction does exactly the same thing not only for horizontal events but also for dipping events. DMO is an intermediate processing step that attempts to position the conflicting dips in the correct zero-offset location such that, after NMO and DMO, CMP stacking will not attenuate crossing events.

So far, these concepts have all been formulated for a constant-velocity medium. For a variable-velocity medium, the transformation from common-offset to zero-offset performed by NMO combined with DMO cannot be split into two separate processes; instead, it forms a single-step process called migration to zero-offset (MZO). In constant-velocity media, $MZO = DMO \cdot NMO$.

To define the parameters involved in the DMO correction, we need to analyze the kinematics of the common-offset reflection of a dipping layer. For a horizontal layer, the reflection point is situated right under the location of the common midpoint (CMP). For the dipping layer sketched in Figure 0.11, the reflection point for the source-receiver ray is **R**. This point is positioned updip relative to the intersection **O** of the zero-offset ray from the common-midpoint **F** with the dipping reflector.

In a common-offset section, the trace corresponding to a source positioned at point **A** and a receiver positioned at point **B** is placed in the location of the CMP. However, in a zero-offset experiment, the reflection point **R** is observed from the surface position **J**. Migration to zero-offset ($DMO \cdot NMO$) is the transformation that relocates a reflection point in a common-offset section to a corresponding place in a zero-offset section.

In order to define the DMO operator, we must calculate the time correction and the surface coordinate correction that transform a common-offset section into a zero-offset section. In Figure 0.11 the segment **JR** represents the zero-offset ray from the

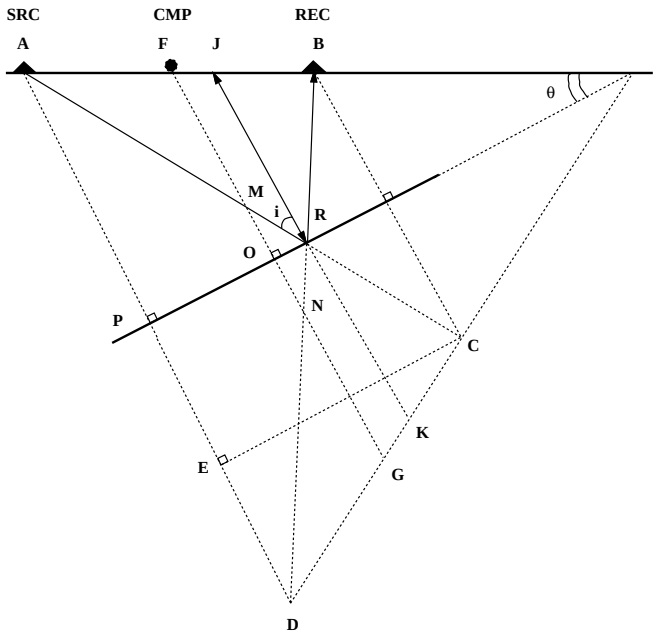

Figure 0.11: DMO kinematics: dipping reflector in a constant velocity medium. The dipping angle is θ. The raypath from the source to the receiver is represented by the segments **AR** and **RB**. The reflection point **R** in the case of a zero-offset experiment that is situated at the surface point **J**. The zero-offset raypath from **J** is equal to the segment **JK**. The incidence angle at **R** is i. intro-dmofig2 [NR]

reflection point **R**. The segment **FJ** represents the surface correction from the CMP to the real zero-offset position of both the source and the receiver. We can calculate the surface correction and the traveltime correction using some elementary geometry.

The source-receiver traveltime t_h corresponds to the ray path **ARB**. The velocity of the medium is v, and the common-offset traveltime is

$$t_h = \frac{(\mathbf{AR} + \mathbf{RB})}{v}.$$

The segment **AB** represents the offset between the source and receiver, and we define the variable h as half the distance between the source and the receiver:

$$\mathbf{AF} = \mathbf{FB} = \frac{\mathbf{AB}}{2} = h.$$

The segment **AC** is equal to **AR** +**RB**, and therefore $\mathbf{AC} = vt_h$.

In Figure 0.11, we can relate the angle of the dipping reflector and the incidence angle of the common-offset raypath through the segment **EC**, as follows

$$\mathbf{EC} = 2h\cos\theta = vt_h \sin i, \tag{0.5}$$

where θ is the dipping angle of the reflector, and i is the incident angle of the common-offset raypath at the reflection point **R**. Squaring equation (0.5) and replacing the

sine by the equivalent cosine expression yields the following equation for the cosine of the incidence angle:

$$\cos i = \frac{1}{vt_h}\sqrt{(vt_h)^2 - (2h\cos\theta)^2}.$$

To obtain the length of the segment $x_0 = \mathbf{FJ}$, which is the DMO surface correction, we must first note that the length of the segment **FJ** is related to the length of the segment **OR** by the relation

$$x_0 = \frac{\mathbf{OR}}{\cos\theta},$$

and further that the segment **OR** in the triangle **ORM** is given by the simple trigonometric relation

$$\mathbf{OR} = \mathbf{MO}\tan i.$$

The segment **MN**= 2**MO** is calculated as half the difference between the bases of the trapezoid **ABCD** as follows:

$$\mathbf{MO} = \frac{\mathbf{MN}}{2} = \frac{\mathbf{AD} - \mathbf{BC}}{4} = h\sin\theta. \tag{0.6}$$

Finally using the three previous relationships we can get the length of the surface correction x_0 as a function of the dip angle, half-offset, medium velocity, and traveltime:

$$x_0 = \frac{\mathbf{OR}}{\cos\theta} = \mathbf{MO}\frac{\tan i}{\cos\theta} = h\sin\theta\frac{\tan i}{\cos\theta} = \frac{2h^2\sin\theta}{\sqrt{(vt_h)^2 - (2h\cos\theta)^2}}. \tag{0.7}$$

The zero-offset traveltime represented by the segment **JK** is given in the trapezoid **FJKG** by the equation

$$\mathbf{JK} = \mathbf{FG} - 2\mathbf{FJ}\sin\theta, \tag{0.8}$$

where we know the length of the segment $x_0 = \mathbf{FJ}$ from equation (0.7), and the length of the other segment **FG** from equation (0.2):

$$\mathbf{FG} = \sqrt{(vt_h)^2 - (2h\cos\theta)^2}.$$

Substituting the expressions of **FG** and **FJ** into equation (0.8) and dividing by the medium velocity, we can calculate the zero-offset travel time as follows:

$$t_0 = \frac{\mathbf{JK}}{v} = \frac{(vt_h)^2 - (2h)^2}{v\sqrt{(vt_h)^2 - (2h\cos\theta)^2}}. \tag{0.9}$$

Thus, if we group together equations (0.7) and (0.9), the parametric equations defining the $MZO = DMO \cdot NMO$ operator in constant velocity media become

$$\begin{cases} x_0 = \dfrac{2h^2 \sin\theta}{v\sqrt{t_h^2 - \frac{4h^2}{v^2}\cos^2\theta}} \\ \\ t_0 = \dfrac{t_h^2 - \frac{4h^2}{v^2}}{\sqrt{t_h^2 - \frac{4h^2}{v^2}\cos^2\theta},}. \end{cases} \tag{0.10}$$

The formulas in equation (0.10) tell us where an event from a common-offset section is moved in a zero-offset section when the dip is known. However, as the next section shows, we do not have to know the dip angle to apply the DMO operator correctly. Figure 0.12 shows the variation of t_0 and x_0 for a whole range of dips. For a zero dip, we have

$$\begin{cases} x_0 = 0 \\ \\ t_0 = \sqrt{t_h^2 - \left(\dfrac{2h}{v}\right)^2} \end{cases}$$

which is precisely the NMO correction.

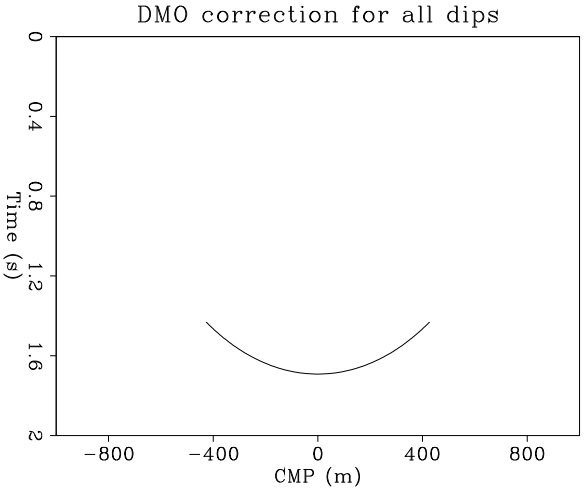

Figure 0.12: Distribution of the DMO correction for all dips ($\frac{-\pi}{2} \leq \theta \leq \frac{\pi}{2}$). intro-MZOimpulse [ER]

0.3.4 How DMO processing works

The goal of the MZO ($DMO \cdot NMO$) processing step is to transform a common-offset section into a zero-offset section. We can conceive of any structure (or depth model) as composed of independent diffractors. This is the commonplace assumption for Kirchhoff migration. By summing the contributions from all the diffractors we can obtain a common-offset section. Following this hypothesis, it is interesting to examine

the behavior of a single diffraction curve in a common-offset section. Figure 0.13 shows a common-offset diffraction curve together with a zero-offset diffraction curve that is actually a hyperbola. The aim of the $DMO \cdot NMO$ step is to transform the common-offset into the zero-offset curve.

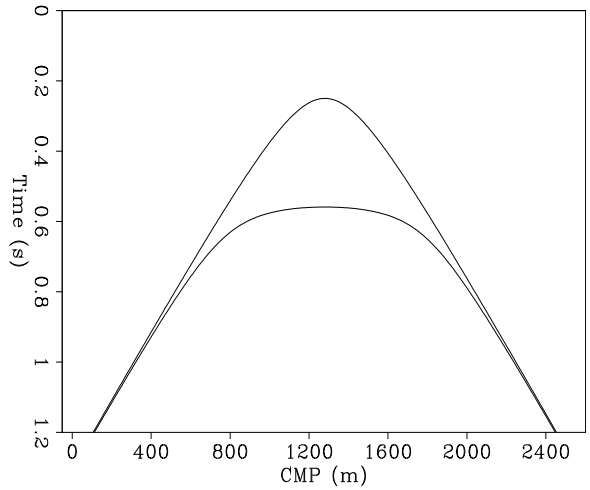

Figure 0.13: Zero-offset hyperbola and the common-offset diffraction curve. intro-cozo [ER]

Figure 0.14 shows the kinematics of the $DMO \cdot NMO$ operator; each point along the common-offset diffraction curve is spread along an operator similar to the one shown in Figure 0.12 that uses equation (0.10). The result of this operation appears on the right side of Figure 0.14. The artifacts at the top of the figure result from the constant amplitude assigned along the DMO curve. In reality, the amplitude along the DMO curve is tapered toward the end of the operator.

For a better understanding of DMO kinematic properties, the reader may find it amusing to solve the two geometry problems that follow.

Problem 1.

Demonstrate that for the geometry presented in Figure 0.11 the following equality is true:

$$\frac{\mathbf{AD}}{\mathbf{FG}} = \frac{\mathbf{JK}}{\mathbf{BC}}.$$

Problem 2.

For the geometry presented in Figure 0.11, and using equation (0.6), show that the reflection point displacement measured along the reflector is

$$\mathbf{OR} = \frac{h^2}{v t_{cmp}} 2 \sin\theta \cos\theta, \tag{0.11}$$

where t_{cmp} is the traveltime from the CMP location (point **F**) to the reflector and back (or the segment **FG** in time units), and v is the medium velocity. The length of

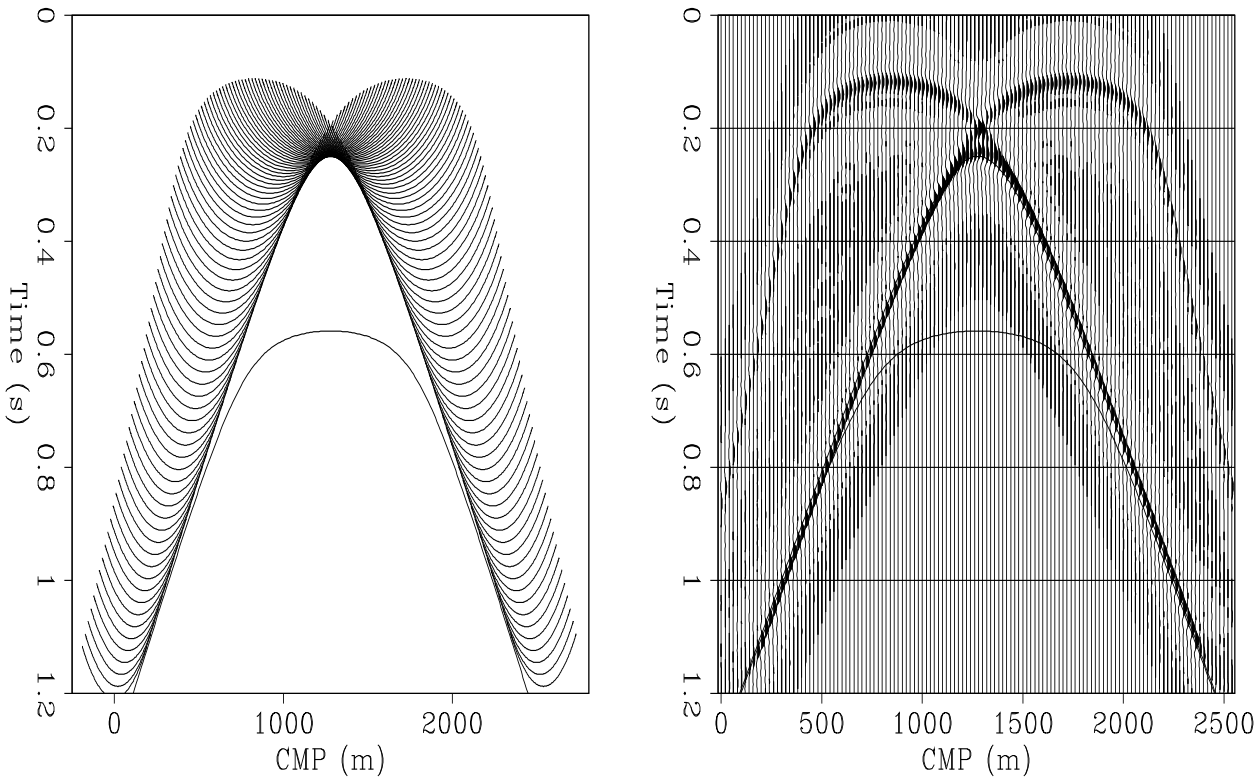

Figure 0.14: The transformation of a common-offset diffraction curve to a zero-offset hyperbola by $DMO \cdot NMO$.
a. $DMO \cdot NMO$ kinematics. Each point on the common-offset diffraction curve is shifted with the NMO correction and spread along the DMO curve.
b. The result of applying $DMO \cdot NMO$ to the common-offset hyperbola. The artifacts result from using a constant amplitude along the DMO curve. intro-codmo [ER]

the segment **FG** is given in equation (0.2). Equation (0.11) appears in Levin's (1971) classic paper, and is also the first equation Hale uses when explaining DMO in his Society of Exploration Geophysicists course notes.

0.4 DMO by Fourier transform

Until now we have examined only the kinematics of the DMO and NMO operators. The amplitudes of the DMO operator are gracefully handled by a new type of dip-moveout processing: DMO by Fourier transform, introduced in the next section. Even though the first definition of DMO by Fourier transform also uses only kinematic arguments, Chapter 2 shows that the amplitude of the operator is very close to the one obtained analytically from the wave equation.

0.4.1 2-D Fourier transforms of dipping events

In order to understand how DMO by Fourier transform works, we have to examine some properties of the 2-D Fourier transform. It is particularly important that all events with a particular slope in the time-space domain are mapped to a single radial line (a line passing through the origin) in the frequency-wavenumber domain. In other words a segment with slope $\frac{\Delta t}{\Delta y}$ is mapped in Fourier domain in a segment with slope $\frac{k_y}{\omega}$.

A two-dimensional function representing a segment of constant amplitude in a zero-offset section can be described by

$$H(y)\delta(\frac{t-t_0}{p}-y),$$

where

$$\begin{cases} H(y)=1; & y\in[a,b] \\ \\ H(y)=0; & y\in(-\infty,a)\cup(b,\infty), \end{cases}$$

t and y are the zero-offset coordinates, t_0 is the intersection point on the time axis, and the value p is the tangent of the slope

$$p=\tan\alpha=\frac{\Delta t}{\Delta y}.$$

In the corresponding depth model, p becomes

$$p=\frac{\Delta t}{\Delta y}=\frac{2\sin\theta}{v},$$

as Figure 0.15 shows. The angle θ represents the slope of the reflector in the depth model, and v is the velocity of the medium. The function $\delta(\frac{t-t_0}{p}-y)$ has unitary amplitude when the argument is zero or $y=\frac{t-t_0}{p}$.

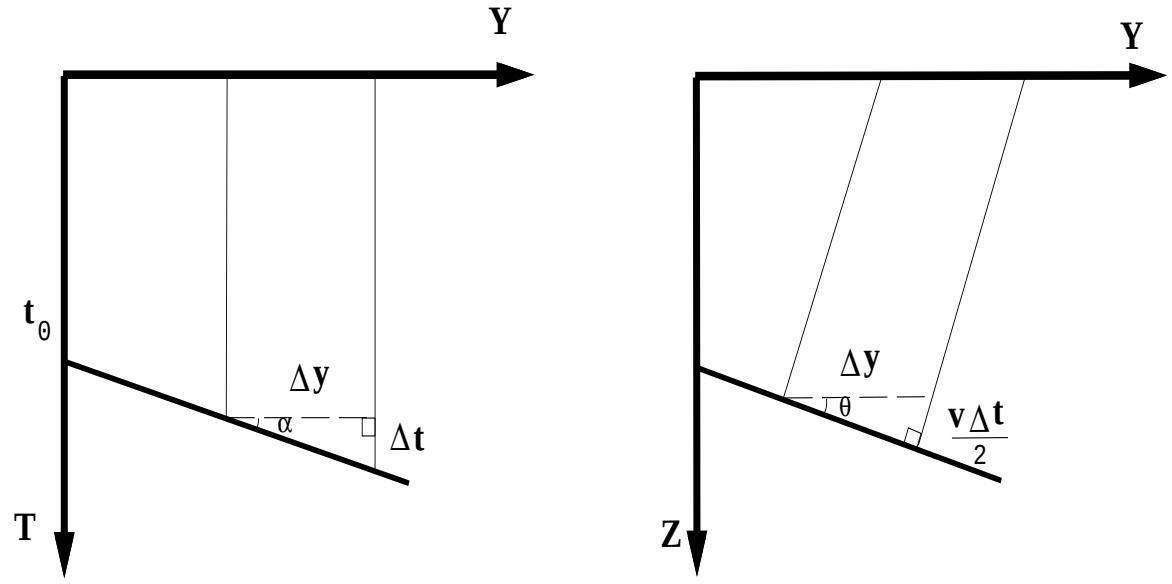

Figure 0.15: Dipping-bed geometry in a common-offset section and the corresponding constant velocity depth model. In a zero-offset section, the slope of the reflection is $\Delta t/\Delta y = 2\sin\theta/v$, where θ is the dipping angle in the depth model, and v is the velocity. intro-dipkxomega [NR]

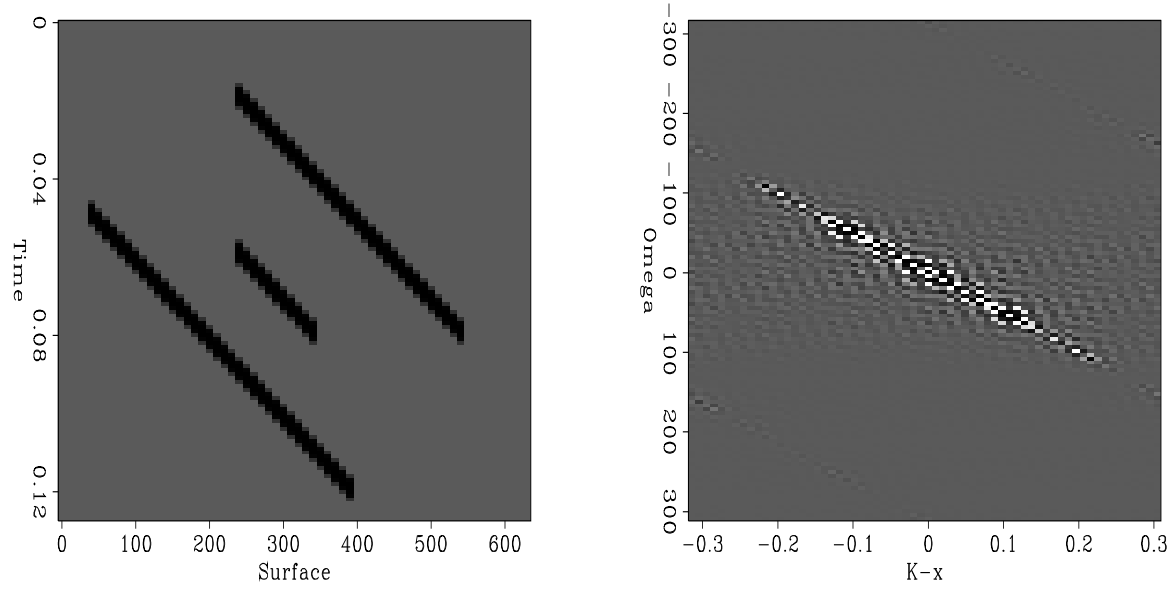

Figure 0.16: The effect of 2-D Fourier transform on events with same dip.
a. Several reflectors with the same dip in space-time coordinates.
b. The 2-D Fourier transform of the same section. All the events are mapped on a radial line. intro-FFT2Ddips [ER]

The Fourier transform of a finite segment differs from that of an infinitely long segment only in the amplitude term. This is to be expected since we actually multiply the infinite segment by a boxcar filter, which in the Fourier domain means convolve it with a sync function. The 2-D Fourier transform of an infinite segment is

$$\begin{aligned} S(\omega, k_y) &= \int dt\, e^{i\omega t} \int dy\, e^{-ik_y y} \delta(\frac{t - t_0}{p} - y) \\ &= \int dt\, e^{i\omega t} e^{-ik_y \frac{t-t_0}{p}} \\ &= e^{i\frac{k_y t_0}{p}} \delta(\omega - \frac{k_y}{p}), \end{aligned}$$

which in the ω, k_y space represents a line with slope

$$\frac{k_y}{\omega} = p = \frac{dt}{dy} = \frac{2\sin\theta}{v}. \tag{0.12}$$

Figure 0.16.a shows several dipping segments with the same slope that, after the Fourier transformation, are all mapped to a radial line in ω, k_y space, as displayed in Figure 0.16.b.

0.4.2 Hale's DMO

Given the geometry in Figure 0.17, as proved in the preceding section,

$$t_0^2 = t_h^2 - \left(\frac{2h\cos\theta}{v}\right)^2, \tag{0.13}$$

where t_0 is the traveltime from the CMP to the reflector and back, t_h is the source-receiver traveltime, $2h$ is the distance between source and receiver, and v is the velocity of the medium. In this situation the reflection point **R** in the nonzero-offset case differs from the actual reflection point **S** in the zero-offset case.

Hale (1984) uses equation (0.13) to write

$$t_0^2 = t_h^2 - \frac{4h^2}{v^2} + \frac{4h^2\sin^2\theta}{v^2}, \tag{0.14}$$

where the NMO corrected time is

$$t_n^2 = t_h^2 - \frac{4h^2}{v^2}. \tag{0.15}$$

Substituting t_n in equation (0.14), we have

$$t_0^2 = t_n^2 + \frac{4h^2\sin^2\theta}{v^2}. \tag{0.16}$$

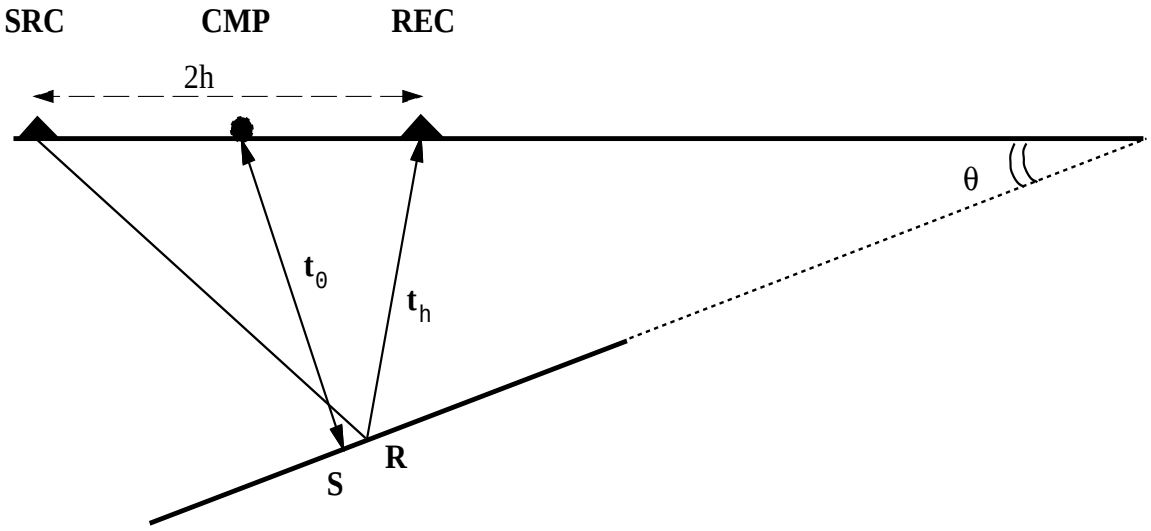

Figure 0.17: Geometry for a dipping reflector in a constant velocity medium. The reflection point for the nonzero-offset ray **R** is different from the zero-offset reflection point **S**. The dipping angle is θ. intro-HaleDMO [NR]

Let us consider a pressure field $p(t_h, y, h)$ recorded as a function of nonzero-offset time t_h, midpoint y, and offset h. In a common-offset section we set the variable h to a constant value, which gives us a 2-D field $p(t_h, y; h = h_0)$. For all the values of the offset h, we have a 3-D field $p(t_h, y; h)$. We define a new field $p_n(t_n, y, h)$ as

$$p_n(t_n, y, h) \equiv p(\sqrt{t_n^2 + \frac{4h^2}{v^2}}, y, h), \tag{0.17}$$

replacing the value of the common-offset traveltime t_h in $p(t_h, y, h)$ by its expression in equation (0.15):

$$t_h^2 = t_n^2 + \frac{4h^2}{v^2}.$$

Note that for a constant value of h this transformation amounts to shifting a value in a trace from t_h to t_n.

Next we define another field $p_0(t_0, y, h)$ as

$$p_0(t_0, y, h) \equiv p_n(\sqrt{t_0^2 - \frac{4h^2 \sin^2\theta}{v^2}}, y, h), \tag{0.18}$$

by replacing the value of the NMO-corrected traveltime t_n in $p_n(t_n, y, h)$ with its expression in equation (0.16). Equation (0.18) is dip-dependent because it contains the variable $\sin\theta$. So far the new field $p_0(t_0, y, h)$ is unknown; further computations are needed to determine it. However, equation (0.18) formally represents a mapping from an NMO-corrected field to a DMO-corrected field. It is important to keep in mind that in this formulation the nonzero-offset reflection point **R** does not correspond to the zero-offset reflection point **S**.

Thus the only variable in equation (0.18) that we cannot easily determine is $\sin\theta$, so we need to find a transformation to express $\sin\theta$ as a function of the other variables. In a zero-offset section

$$\sin\theta = \frac{v\Delta t_0}{2\Delta y},$$

as shown in Figure 0.15. However, in equation (0.12) we proved that for a dipping segment we have a relationship between $\sin\theta$ and the ratio of the midpoint wavenumber and frequency:

$$\frac{dt_0}{dy} = \frac{k_y}{\omega_0} = \frac{2\sin\theta}{v}. \tag{0.19}$$

Now we need to Fourier transform the pressure field $p_0(t_0, y, h)$ to take advantage of the new variables k_y and ω used in equation (0.19) as follows:

$$P_0(\omega_0, k_y, h) = \int_{t_0} dt_0 \int_y dy e^{i(\omega_0 t_0 - k_y y)} p_0(t_0, y, h). \tag{0.20}$$

We can now use the mapping defined in equation (0.18) to replace $p_0(t_0, y, h)$ in equation (0.20) with $p_n(t_n, y, h)$. Changing the variable of integration requires calculating the Jacobian of the transformation (0.16). Rewriting the zero-offset time from equation (0.16) as

$$t_0 = \sqrt{t_n^2 + h^2\frac{k_y^2}{\omega_0^2}},$$

and derivating with respect to t_n provides the Jacobian

$$J = \left[\frac{dt_0}{dt_n}\right] = \frac{t_n}{\sqrt{t_n^2 + h^2\frac{k_y^2}{\omega_0^2}}}. \tag{0.21}$$

We can now rewrite equation (0.20) as

$$P_0(\omega_0, k_y, h) = \int_{t_n} dt_n \int_y d_y \frac{t_n}{\sqrt{t_n^2 + h^2\frac{k_y^2}{\omega_0^2}}} p_n(t_n, y, h) e^{i(\omega_0\sqrt{t_n^2 + h^2\frac{k_y^2}{\omega_0^2}} - k_y y)}, \tag{0.22}$$

which is Hale's DMO by Fourier transform.

0.4.3 Zhang's improved DMO

Zhang (1988) observed that in Hale's DMO, the reflection point in the nonzero-offset case does not coincide with the reflection point in the zero-offset case. He has derived a new formula for DMO that takes into account not only a time correction but also a midpoint correction. Zhang's derivation of the new DMO correction introduces a different Jacobian for the DMO operator. In other words, the kinematics of the operator are identical, but the amplitude along the operator differs. Zhang starts by

examining the time and midpoint corrections obtained in section 0.2.3. The $DMO \cdot NMO$ correction in constant velocity media, from equation (0.10), is

$$\begin{cases} \Delta y_0 = \dfrac{2h^2 \sin\theta}{v\sqrt{t_h^2 - 4h^2 \frac{\cos^2\theta}{v^2}}} \\ \\ t_0 = \dfrac{t_h^2 - \frac{4h^2}{v^2}}{\sqrt{t_h^2 - 4h^2 \frac{\cos^2\theta}{v^2}}}. \end{cases}$$

We can isolate the NMO transformation, which is only a time-shift,

$$t_n^2 = t_h^2 - \frac{4h^2}{v^2},$$

and write for the DMO operator

$$\begin{cases} y_0 = y - \dfrac{2h^2 \sin\theta}{v\sqrt{t_n^2 + 4h^2 \frac{\sin^2\theta}{v^2}}} \\ \\ t_0 = \dfrac{t_n^2}{\sqrt{t_n^2 + 4h^2 \frac{\sin^2\theta}{v^2}}}. \end{cases} \tag{0.23}$$

In equation (0.23) the y axis increases to the left, and the angles are positive if they dip toward the right and negative if they dip toward the left. In Figure 0.18 the angle θ is negative, which can also be derived from equation (0.19), as follows:

$$\frac{dt_0}{dy_0} = \frac{2\sin\theta}{v},$$

where the sign of dy_0 determines the sign of the angle.

The next steps define another field $p_0(t_0, y_0, h)$ by extending Hale's reasoning to the case in which not only the time variable but also the common-midpoint variable is changed. The common-midpoint change accounts for the fact that the DMO transformation defined by Zhang moves the nonzero-offset reflection point to a zero-offset reflection point. Stacking after this transformation produces true common-depth-point gathers. In the transformation Hale defined, the reflection point for the nonzero-offset is different from that in the zero-offset case.

After introducing the two new variables in the zero-offset field and renaming the zero-offset time and midpoint coordinates t_0 and y_0, the Fourier transform of the new field is

$$P_0(\omega_0, k_{y_0}, h) = \int_{t_0} dt_0 \int_{y_0} dy_0 \; e^{i(\omega_0 t_0 - k_{y_0} y_0)} p_0(t_0, y_0, h). \tag{0.24}$$

We then replace the variables t_0 and y_0 in equation (0.24) with the known variables t_n and y. Fortunately, it is not necessary to express explicitly $t_n = t_n(t_0, y_0)$ and

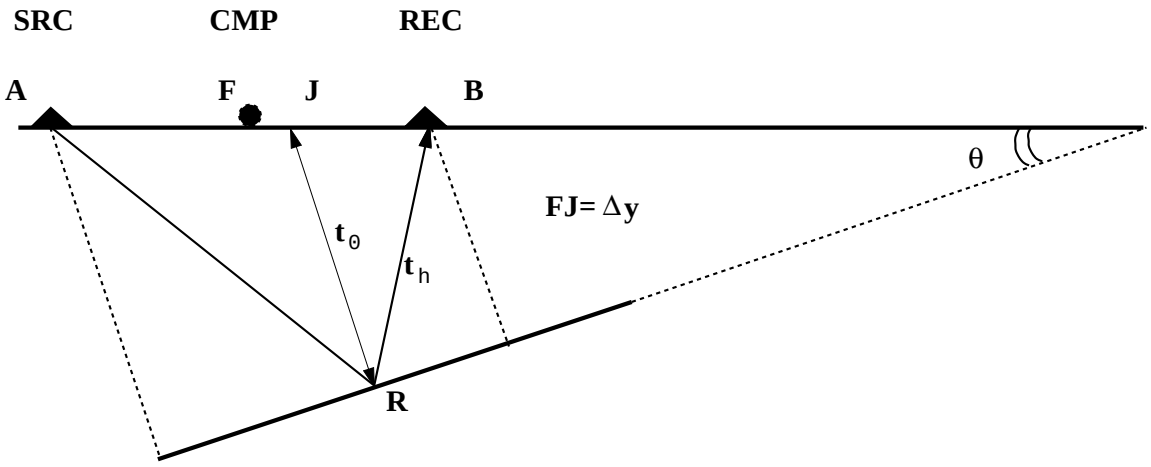

Figure 0.18: Geometry for a dipping reflector in a constant velocity medium. The reflection point for the nonzero-offset ray **R** is the same as the one for the zero-offset ray **JR**. The dipping angle is θ. intro-ZhangDMO [NR]

$y = y(t_0, y_0)$, though we assume the respective dependencies. Differentiating equation (0.23), we find the differentials of the new variables

$$\begin{cases} dy_0 = dy \\ \\ dt_0 = \dfrac{t_n(t_n^2 + 8h^2\frac{\sin^2\theta}{v^2})}{(t_n^2 + 4h^2\frac{\sin^2\theta}{v^2})^{\frac{3}{2}}} dt_n \end{cases} \tag{0.25}$$

and introduce them into equation (0.24). Using the equality (0.19) we replace the expression

$$\frac{2\sin\theta}{v} \quad \text{with the equivalent expression} \quad \frac{k_{y_0}}{\omega_0}.$$

The phase becomes

$$\begin{aligned} \Phi &= \omega_0 t_0 - k_{y_0} y_0 \\ &= \omega_0 \frac{t_n^2}{\sqrt{t_n^2 + h^2\frac{k_{y_0}^2}{\omega_0^2}}} - k_{y_0}(y - \frac{h^2 k_{y_0}}{\omega_0\sqrt{t_n^2 + h^2\frac{k_{y_0}^2}{\omega_0^2}}}) \\ &= \omega_0\sqrt{t_n^2 + h^2\frac{k_{y_0}^2}{\omega_0^2}} - k_{y_0} y, \end{aligned}$$

which is the same phase as in Hale's equation (0.22).

Equation (0.24) then becomes

$$P_0(\omega_0, k_{y_0}, h) = \int_{t_n} dt_n \int_y dy \frac{t_n(t_n^2 + 2h^2\frac{k_{y_0}^2}{\omega_0^2})}{(t_n^2 + h^2\frac{k_{y_0}^2}{\omega_0^2})^{\frac{3}{2}}} p(t_n, y, h) e^{i(\omega_0\sqrt{t_n^2 + h^2\frac{k_{y_0}^2}{\omega_0^2}} - k_{y_0} y)}. \tag{0.26}$$

Comparison of equation (0.26) with Hale's equation (0.22) shows that they only differ in the amplitude term. The two Jacobians are

$$J_H = \frac{t_n}{\sqrt{t_n^2+h^2\frac{k_{y_0}^2}{\omega_0^2}}}$$

and

$$J_Z = \frac{t_n(t_n^2+2h^2\frac{k_{y_0}^2}{\omega_0^2})}{(t_n^2+h^2\frac{k_{y_0}^2}{\omega_0^2})^{\frac{3}{2}}}.$$

The ratio between the Jacobians is

$$\frac{J_Z}{J_H} = \frac{t_n^2+2h^2\frac{k_{y_0}^2}{\omega_0^2}}{t_n^2+h^2\frac{k_{y_0}^2}{\omega_0^2}}. \tag{0.27}$$

0.4.4 MZO by Fourier transform

Both Hale and Zhang separate the NMO correction from the DMO correction. However, for variable velocity media we cannot do this. Rather, in order to generalize the $DMO \cdot NMO$ operation, we have to use the migration to zero-offset (MZO) concept. The next chapter treats this subject in detail, but here, for the sake of consistency, I include the simple case of MZO by Fourier transform. The Fourier transform expression is simply obtained by using equation (0.23) without separating the NMO step, as follows:

$$\begin{cases} y_0 = y - \dfrac{2h^2\sin\theta}{v\sqrt{t_h^2-\frac{4h^2}{v^2}+4h^2\frac{\sin^2\theta}{v^2}}} \\ \\ t_0 = \dfrac{t_h^2-\frac{4h^2}{v^2}}{\sqrt{t_h^2-\frac{4h^2}{v^2}+4h^2\frac{\sin^2\theta}{v^2}}}. \end{cases} \tag{0.28}$$

The differentials of the new variables are

$$\begin{cases} dy_0 = dy \\ \\ dt_0 = \dfrac{t_h(t_h^2-\frac{4h^2}{v^2}+2h^2\frac{k_{y_0}^2}{\omega_0^2})}{(t_h^2-\frac{4h^2}{v^2}+h^2\frac{k_{y_0}^2}{\omega_0^2})^{\frac{3}{2}}}dt_h, \end{cases} \tag{0.29}$$

and by replacing the variables y_0 and t_0 in equation (0.24), we obtain

$$P_0(\omega_0,k_{y_0},h) = \int_{t_h}dt_h\int_y dy\frac{t_h(t_h^2-\frac{4h^2}{v^2}+2h^2\frac{k_{y_0}^2}{\omega_0^2})}{(t_h^2-\frac{4h^2}{v^2}+h^2\frac{k_{y_0}^2}{\omega_0^2})^{\frac{3}{2}}}p(t_h,y,h)\,e^{i(\omega_0\sqrt{t_h^2-\frac{4h^2}{v^2}+h^2\frac{k_{y_0}^2}{\omega_0^2}}-k_{y_0}y)}. \tag{0.30}$$

Note that replacing the quantity

$$t_h^2 - \frac{4h^2}{v^2}$$

in equation (0.30) with t_n^2 gives us the same phase as the one obtained by Hale and Zhang, but the Jacobian differs from Zhang's Jacobian by a factor of

$$\frac{J_M}{J_Z} = \frac{t_h}{t_n} = \sqrt{1 + \frac{4h^2}{v^2 t_n^2}}, \tag{0.31}$$

which corresponds to the Jacobian of the NMO transformation.